Long-term in vivo microscopy of CAR T cell dynamics during eradication of CNS lymphoma in mice

Matthias Mulazzani[a,1], Simon P. Fräßle[b,c], Iven von Mücke-Heim[a], Sigrid Langer[a], Xiaolan Zhou[a,d], Hellen Ishikawa-Ankerhold[e], Justin Leube[b], Wenlong Zhang[a], Sarah Dötsch[b], Mortimer Svec[b], Martina Rudelius[f], Martin Dreyling[g], Michael von Bergwelt-Baildon[g], Andreas Straube[a], Veit R. Buchholz[b], Dirk H. Busch[b,c,2], and Louisa von Baumgarten[a,1,2]

[a]Department of Neurology, Ludwig Maximilians University, 81377 Munich, Germany; [b]Institute for Medical Microbiology, Immunology and Hygiene, Technical University of Munich, 81675 Munich, Germany; [c]Institute for Advanced Study, Technical University of Munich, 85748 Garching, Germany; [d]Department of Rehabilitation, Shengjing Hospital of China Medical University, Shenyang 110022, China; [e]Department of Internal Medicine I, Ludwig Maximilians University, 81377 Munich, Germany; [f]Institute of Pathology, Ludwig Maximilians University, 80337 Munich, Germany; and [g]Department of Internal Medicine III, Ludwig Maximilians University, 81377 Munich, Germany

Edited by Michael B. A. Oldstone, Scripps Research Institute, La Jolla, CA, and approved October 10, 2019 (received for review March 5, 2019)

T cells expressing anti-CD19 chimeric antigen receptors (CARs) demonstrate impressive efficacy in the treatment of systemic B cell malignancies, including B cell lymphoma. However, their effect on primary central nervous system lymphoma (PCNSL) is unknown. Additionally, the detailed cellular dynamics of CAR T cells during their antitumor reaction remain unclear, including their intratumoral infiltration depth, mobility, and persistence. Studying these processes in detail requires repeated intravital imaging of precisely defined tumor regions during weeks of tumor growth and regression. Here, we have combined a model of PCNSL with in vivo intracerebral 2-photon microscopy. Thereby, we were able to visualize intracranial PCNSL growth and therapeutic effects of CAR T cells longitudinally in the same animal over several weeks. Intravenous (i.v.) injection resulted in poor tumor infiltration of anti-CD19 CAR T cells and could not sufficiently control tumor growth. After intracerebral injection, however, anti-CD19 CAR T cells invaded deeply into the solid tumor, reduced tumor growth, and induced regression of PCNSL, which was associated with long-term survival. Intracerebral anti-CD19 CAR T cells entered the circulation and infiltrated distant, nondraining lymph nodes more efficiently than mock CAR T cells. After complete regression of tumors, anti-CD19 CAR T cells remained detectable intracranially and intravascularly for up to 159 d. Collectively, these results demonstrate the great potential of anti-CD19 CAR T cells for the treatment of PCNSL.

CAR T cells | PCNSL | 2-photon microscopy | tumor immunology

Primary central nervous system lymphoma (PCNSL) is a highly malignant brain tumor. Although improvement of chemotherapeutic treatment algorithms has led to improved survival (1), up to 30% of patients do not respond to first-line therapy, and more than 50% of patients relapse (2). Treatment options for chemotherapy-refractory and relapsed PCNSL are limited, and the prognosis of these patients is dismal. Therefore, novel therapeutic strategies are urgently needed.

Animal models used for analyzing biological characteristics of PCNSL growth have been successful in mimicking its human counterpart in many aspects (3). However, due to its growth in a hardly accessible organ, dynamic analysis of PCNSL growth and its microenvironment is challenging, rendering detailed analysis of PCNSL growth and potential treatment effects at a single-cell level impossible. Development of an improved murine model of PCNSL combining a chronic cranial window with 2-photon laser scanning microscopy (TPLSM) could significantly enhance our understanding of this disease and potentially curative treatment regimens.

In recent years, one of the most promising novel cancer therapies has been the development of chimeric antigen receptor (CAR) T cells (4). Their most successful example is targeting the B cell lineage-specific surface antigen CD19. Several clinical trials have illustrated their potent antitumor efficacy in systemic B cell malignancies, including peripheral diffuse large B cell lymphoma (DLBCL) (5, 6). Importantly, more than 90% of PCNSL are of the DLBCL subtype, expressing the surface antigen CD19 (7). Recently, a case report illustrated the complete remission of a secondary CNS lymphoma in a patient treated with anti-CD19 CAR T cells (8). However, detailed data about the efficacy of anti-CD19 CAR T cells in the treatment of PCNSL are lacking.

Furthermore, many cellular aspects of CAR T cell therapy remain obscure. In brain tumors, CAR T cells face additional barriers, as the trafficking of immune cells to the brain is tightly regulated and infiltration of immune cells into the tumor core as well as their functional persistence may be impaired due to the highly immunosuppressive tumor microenvironment (9). To circumvent the blood–brain barrier and enhance tumor infiltration, many studies involving brain tumor patients, therefore, apply CAR T cells not intravenously (i.v.) but via intracranial injection. The latter, however,

MEDICAL SCIENCES

Significance

Primary central nervous system lymphoma (PCNSL) is a highly malignant brain tumor with limited treatment options. Here, we show that genetically engineered T cells, expressing a chimeric antigen receptor, thoroughly infiltrate these tumors in mice. Combining intravital 2-photon microscopy with chronic cranial windows, we were able to visualize their intratumoral proliferation and intracerebral persistence for up to 159 d, leading to the eradication of large, established PCNSL and to long-term survival.

Author contributions: M.M., V.R.B., D.H.B., and L.v.B. designed research; M.M., S.P.F., I.v.M.-H., S.L., X.Z., H.I.-A., J.L., W.Z., S.D., M.S., and M.R. performed research; M.D. contributed new reagents/analytic tools; M.M., S.P.F., I.v.M.-H., S.L., J.L., M.R., M.v.B.-B., A.S., V.R.B., and L.v.B. analyzed data; M.D., M.v.B.-B., and A.S. provided clinical as well as methodological input; A.S. provided laboratory infrastructure; and M.M. and L.v.B. wrote the paper.

Competing interest statement: S.P.F., I.v.M.-H., S.L., X.Z., H.I.-A., J.L., W.Z., S.D., M.S., M.R., A.S., V.R.B., and L.v.B. declare that they have no competing interests. M.M. has been a member of a scientific advisory committee for Gilead. M.D. has been a member of a scientific advisory committee for Novartis. M.v.B.-B. received research funding from Miltenyi Biotech and Novartis and honoraria from Kite/Gilead. D.H.B. is cofounder of STAGE cell therapeutics GmbH (now Juno Therapeutics/Celgene) and T Cell Factory B.V. (now Kite/Gilead). D.H.B. has a consulting contract with and receives sponsored research support from Juno Therapeutics. The authors have no additional financial interests.

This article is a PNAS Direct Submission.

This open access article is distributed under Creative Commons Attribution-NonCommercial-NoDerivatives License 4.0 (CC BY-NC-ND).

[1]To whom correspondence may be addressed. Email: matthias.mulazzani@med.uni-muenchen.de or louisa.vonbaumgarten@med.uni-muenchen.de.

[2]D.H.B. and L.v.B. contributed equally to this work.

This article contains supporting information online at www.pnas.org/lookup/suppl/doi:10.1073/pnas.1903854116/-/DCSupplemental.

First published November 11, 2019.

might be associated with an increased procedural risk, and its superiority has not been proven yet.

Although intravital microscopy has provided many crucial findings regarding the CNS recruitment of T cells (10) as well as the extra- and intratumoral movement of tumor-specific cytotoxic T cells (11, 12) and natural killer (NK) cells (13), the detailed behavior of individual tumor-specific CAR T cells might differ significantly (14) and has not been characterized in vivo in brain tumors. Additionally, only limited information exists regarding systemic or intracranial persistence of CAR T cells in the treatment of (brain) malignancies.

Current hypotheses of CAR T cell tumor infiltration patterns, proliferation, and intratumoral migration rely on low-resolution techniques (such as positron emission tomography or bioluminescence imaging), ex vivo analyses, or in vitro experiments, precluding repeated analysis of individual cellular behavior and tumor responses in detail.

To fill this knowledge gap, we developed a mouse model of orthotopic PCNSL growth. This enabled us to repeatedly visualize fluorescent intracerebral $CD19^+$ human lymphoma cells and murine CAR T cells targeting human CD19 in vivo at single-cell resolution using TPLSM through a chronic cranial window. Thereby, we were able to compare the therapeutic effects of i.v. and intracerebral injections of low-dose anti-CD19 CAR T cells on tumor growth in real time. Repeated measurement of tumor size through the chronic cranial window and ex vivo tumor volume measurement demonstrated higher efficacy of regional, intracerebral CAR T cell injection, leading to successful tumor eradication of large, established CNS lymphoma. Using in vivo TPLSM, this model additionally allowed for in-depth analysis of intratumoral and intracerebral CAR T cell behavior and the spatiotemporal aspects of their persistence. Our findings underline the importance of detailed, dynamic surveillance of CAR T cell behavior and illustrate the potent in vivo activity of anti-CD19 CAR T cells in the treatment of PCNSL.

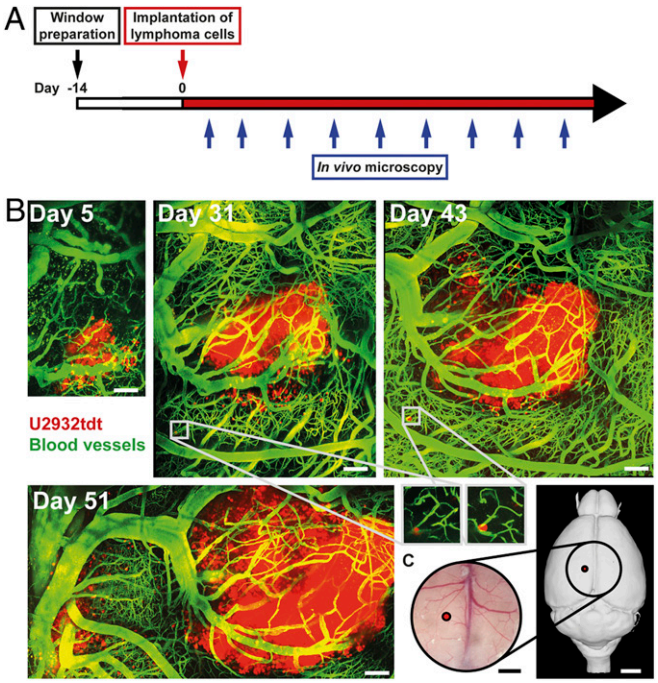

Fig. 1. Characteristic pattern of PCNSL growth repeatedly visualized with in vivo TPLSM. (*A*) Schematic representation illustrating experimental design. (*B*) Intracerebral tumor growth after stereotactic implantation of U2932tdt cells (red). Blood vessels are highlighted after i.v. injection of FITC-dextran (green). Images represent mosaics of multiple maximum intensity projections. *Insets* show perivascular, dormant tumor cells. Representative mosaics of 15 mice from 8 independent experiments. (Scale bars: 100 μm.) (*C*) Position of tumor implantation (red) and position and dimensions of the chronic cranial window (circle; 6 × 6 mm). (Scale bars: *Left*, 1 mm; *Right*, 2 mm.) Right panel created with 3dBAR plugin of the Scalable Brain Atlas (SBA) (53–55).

Results

Development of a Robust In Vivo Model of PCNSL. To gain insight into the pathology of PCNSL, we established a orthotopic mouse model of PCNSL. After stereotactic intracerebral implantation of the $CD19^+$ human DLBCL cell line U2932, $Foxn1^{nu/nu}$ mice lacking functional T cells developed a solid intracerebral tumor with characteristic growth pattern (*SI Appendix*, Fig. S1). Additionally, clusters of lymphoma cells were found infiltrating the brain parenchyma, the periventricular regions, and the leptomeninges (*SI Appendix*, Fig. S1).

Next, we established a red fluorescent lymphoma cell line stably expressing tdTomato (U2932tdt). Microsurgical implantation of a chronic cranial window was well tolerated by mice and enabled us to repeatedly visualize the mouse brain with TPLSM up to a depth of 400 μm (Fig. 1*A*). Thereby, longitudinal visualization of the stereotactically implanted lymphoma cells at single-cell resolution became possible over a period of several weeks.

Initially, the implanted lymphoma cells proliferated slowly. A small cluster of lymphoma cells was found at the injection site (Fig. 1*B*). These cells formed a solitary lesion around preexisting intracerebral blood vessels. Lymphoma cells showed no motility and barely proliferated during real-time videos of up to 2 h; 14 d after cortical implantation, the median visible tumor diameter exceeded 500 μm with angiocentric parenchymal infiltration of single cells and small cell clusters. Detached from the main tumor, several dormant lymphoma cells became visible, residing in a quiescent, nondividing state over periods of several weeks (Fig. 1*B*, *Insets*).

Together, these findings illustrate that stereotactic injection of U2932tdt cells (Fig. 1*C*) leads to successive growth of intracerebral lymphoma. Importantly, this model enabled repeated, detailed visualization of individual intracerebral tumor cells for a period of several weeks.

In Vitro Cytotoxicity of h19m28z CAR T Cells. A meaningful judgement on in vivo functionality and long-term persistence of syngeneic CAR T cells is only possible when preserving physiological cytokine and chemokine production, proliferation, and migration patterns as well as the ability to differentiate into long-lived T cells. Therefore, in designing the CAR, we chose murine transmembrane and costimulatory domains to guarantee all key functional features in this mouse model. Here, we used a newly generated CAR construct recognizing human CD19 linked to murine hinge, transmembrane, and intracellular signaling domains CD28 and CD3 zeta chain (h19m28z). To evaluate the specific cytotoxicity of this newly generated h19m28z CAR, we cocultured transduced and purified (>90%) CAR T cells with $CD19^+$ transduced HEK293 target cells (*SI Appendix*, Fig. S2). To control for potential T cell receptor (TCR)-mediated xenogeneic or unspecific cytotoxicity of murine T cells independent of CAR-mediated effects, we compared the cytotoxicity of h19m28z CAR T cells with the cytotoxicity of mock CAR T cells transduced with a vector without the extracellular binding domain (scFv) necessary for CD19 antigen recognition. Only h19m28z CAR T cells exhibited specific cytotoxicity, whereas mock CAR T cells did not exert any measurable killing activity (*SI Appendix*, Fig. S2 *A* and *B*). Focusing on a specific time point (2 h after addition of effectors), h19m28z CAR T cells show a dose-dependent killing capacity that was not detectable for mock CAR T cells (*SI Appendix*, Fig. S2*C*). These results illustrate the capacity of h19m28z CAR T cells to specifically kill $CD19^+$ cells independent of any bystander cells.

In Vivo CAR T Cell Behavior following i.v. Injection. Next, we sought to analyze intracerebral CAR T cell trafficking and their antitumor efficacy; 14 d after implantation of a chronic cranial window, we implanted U2932tdt cells into the cerebral cortex, which led to the development of large PCNSL 14 d after tumor implantation. Next, we i.v. injected murine h19m28z CAR T cells and regularly performed in vivo TPLSM (Fig. 2*A*). Purity of eGFP$^+$, CAR$^+$ T cells before injection exceeded 98% (*SI Appendix*, Fig. S3). To control for allo- and xenoreactivity and to demonstrate CAR specificity, control mice received mock CAR T cells; 3-dimensional (3D) quantification of intratumoral T cell numbers via TPLSM demonstrated that both mock and h19m28z CAR T cells accumulated intratumorally starting 14 d after i.v. injection, albeit at very low numbers (Fig. 2*B*). Until day 28, the number of intratumoral h19m28z CAR T cells steadily increased.

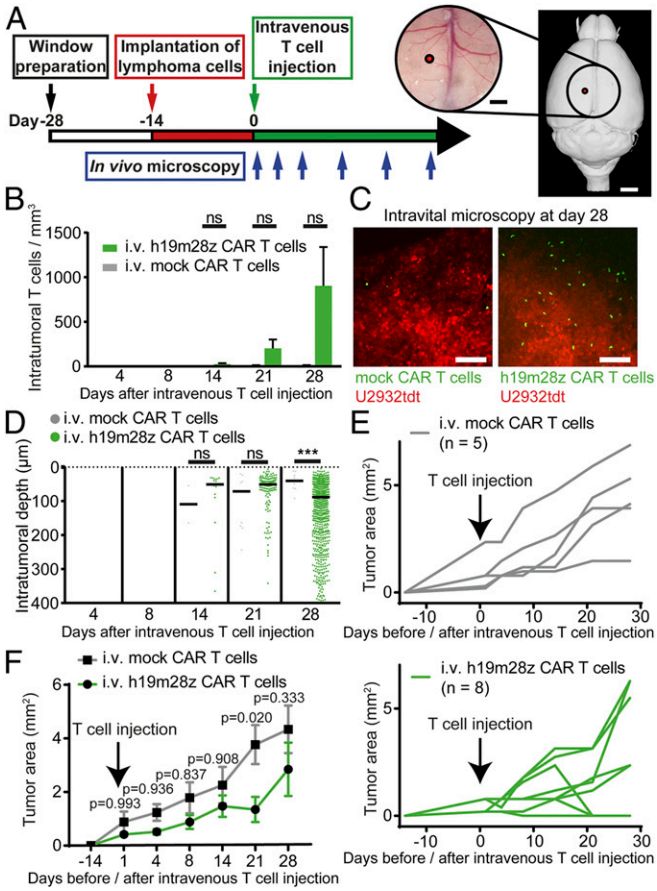

Fig. 2. After i.v. injection, intratumoral h19m28z CAR T cells are present in low numbers without a sustained effect on tumor growth for the majority of treated animals. (*A*) Schematic representation illustrating experimental design. Right panel created with 3dBAR/SBA (53–55). (*B*) Intratumoral mock or h19m28z CAR T cell numbers after i.v. injection (quantification of 1 to 3 3D ROIs per mouse per time point depending on tumor size). (*C*) Representative maximum intensity projections illustrating intratumoral mock (*Left*) and h19m28z CAR T cells (*Right*) 28 d after i.v. injection. (Scale bars: 100 μm.) (*D*) Distance of intratumoral CAR T cells from brain surface (pooled data from 1 to 3 3D ROIs per mouse). Each point represents an individual mock or h19m28z CAR T cell. T cell number and position after tumor regression (day 28: 3 of 8 mice in the h19m28z group, 0 of 5 in the mock group) have been excluded. ***$P < 0.001$. (*E* and *F*) Intracerebral, 2D tumor area assessed by in vivo microscopy after mock and h19m28z CAR T cell treatment. Individual (*E*) and pooled (*F*) tumor size. (*B–F*) $n = 5$ and 8 for mock and h19m28z CAR T cell treatment, respectively, from 4 independent experiments. Data are shown as mean + SEM (*B*) or median (*D*). Mann–Whitney *U* test (*B* and *D*) or 2-way ANOVA followed by Sidak's multiple comparisons test (*F*). ns, not significant.

However, there was no statistical difference compared with mock CAR T cells (Fig. 2 *B* and *C*). A comparatively poor infiltration of the tumor core could be observed for h19m28z CAR T cells from day 14 on. CAR T cells predominantly accumulated in the most superficial intracerebral position (0 to 100 μm) surrounding the subarachnoid space (Fig. 2*D*).

Sequential measurement of intracerebral tumor size revealed reduced tumor growth in animals treated with h19m28z CAR T cells. This effect was significant at day 21, when in 3 of 8 h19m28z CAR T cell-treated mice (37.5%), the tumor regressed (Fig. 2 *E* and *F*). However, due to continuous tumor growth in the remaining 5 animals, there was no statistically significant difference 28 d after CAR T cell injection.

We conclude that i.v. h19m28z CAR T cell injection can lead to tumor regression in a minor fraction of treated mice. However, treatment efficacy is severely impaired by the limited and late recruitment of CAR T cells to the CNS and their poor penetration into the tumor core.

Intratumoral CAR T Cell Density and Distribution after Intracerebral Injection. To overcome the potential drawbacks associated with i.v. application, we next evaluated the effect of intracerebral injections of CAR T cells (Fig. 3*A*). Using this approach, the mean number of intratumoral h19m28z CAR T cells was more than 6-fold higher than after i.v. injection (although the number of intracerebrally injected cells was 7-fold lower). Throughout the observational period of 4 wk, the number of intratumoral h19m28z CAR T cells consistently exceeded the number of intratumoral mock CAR T cells (Fig. 3 *B–D* and Movies S1 and S2). h19m28z CAR T cells reached a maximum intratumoral number at day 21, while mock CAR T cell number already peaked at day 8. At all time points, h19m28z CAR T cells distributed evenly throughout the whole tumor (Fig. 3 *C* and *E*). Contrarily, mock CAR T cells were predominantly accumulating at the most superficial intracerebral position (Fig. 3 *D* and *E*). Deep inside the tumor (>100 μm beneath the most superficial tumor cells), h19m28z CAR T cells were present more numerously than mock CAR T cells at all time points (Fig. 3*E*).

Even 100 μm below the most superficial tumor cells, mock CAR T cells accumulated in higher numbers peritumorally (at the lateral tumor margin) than intratumorally, whereas h19m28z CAR T cells were present at higher numbers intratumorally than peritumorally (*SI Appendix*, Fig. S4), further confirming effective tumor infiltration of h19m28z CAR T cells after intracerebral injection.

Contralateral CAR T Cell Density and Distribution after Intracerebral Injection. In the contralateral, initially tumor- and CAR T cell-free brain hemisphere, the kinetics of intracranial CAR T cell numbers exhibited similar dynamics, although at overall lower numbers compared with intratumoral numbers (*SI Appendix*, Fig. S5*A*). During the first 14 d after injection, there was no significant difference between contralateral h19m28z and mock CAR T cell numbers; 21 d after injection, mock CAR T cells disappeared, while h19m28z CAR T cells persisted for more than 28 d. On day 28, the region of interest (ROI) contralateral to tumor injection was overgrown by tumor in 3 of 4 mice (75%), precluding a valid determination of intraparenchymal, contralateral mock CAR T cell numbers. Initially, both mock and h19m28z CAR T cells accumulated in the arachnoid/subarachnoid compartment (*SI Appendix*, Fig. S5 *B* and *C*). Starting at day 14, h19m28z CAR T cells additionally infiltrated deeper regions of the brain parenchyma and remained visible in deeper intracerebral regions for more than 28 d, whereas mock CAR T cells disappeared after 21 d and did not infiltrate the tumor-free brain parenchyma (i.e., >100 μm below the arachnoid trabeculae) (*SI Appendix*, Fig. S5 *D* and *E*).

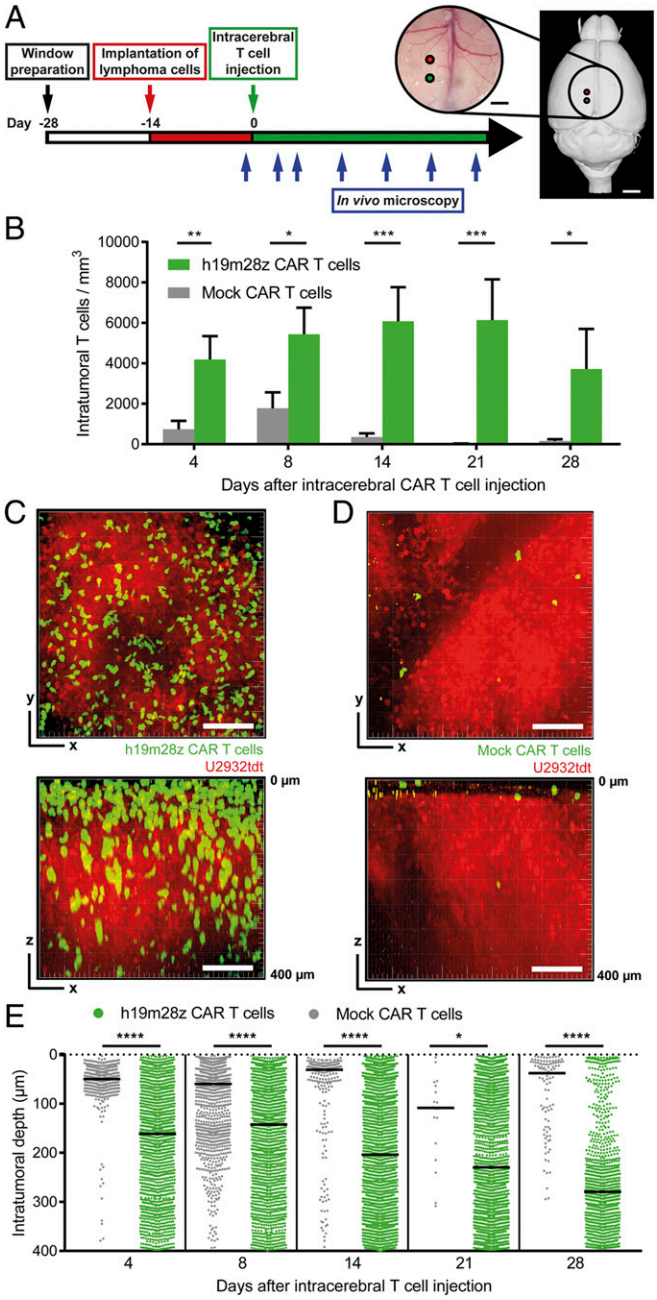

Fig. 3. After intracerebral injection, intratumoral h19m28z CAR T cells are present at higher numbers and persist longer than mock CAR T cells. (*A*) Schematic representation illustrating experimental design. Right panel created with 3dBAR/SBA (53–55). (*B*) Intratumoral CAR T cell numbers in mice treated with intracerebral mock or h19m28z CAR T cells. Quantification of 1 to 2 3D ROIs (depending on tumor size) per mouse. $n = 4$ mice per group from 2 independent experiments. (*C* and *D*) Representative maximum intensity projections of axial (*xy*; *Upper*) and sagittal (*xz*; *Lower*) orientation illustrating intratumoral h19m28z (*C*) and mock (*D*) CAR T cells 14 d after CAR T cell injection. (Scale bars: 100 μm.) (*E*) Distance of intratumoral CAR T cells from brain surface. $n = 1$ to 2 3D ROIs of 4 mice per group from 2 independent experiments. Each point represents an individual mock or h19m28z CAR T cell. T cell number and position after tumor regression (day 28: 2 of 4 mice in the h19m28z group, 0 of 4 in the mock group) have been excluded. Data are shown as mean + SEM (*B*) or median (*E*). Mann–Whitney *U* test (*B* and *E*). ns, not significant. $^*P < 0.05$; $^{**}P < 0.01$; $^{***}P < 0.001$; $^{****}P < 0.0001$.

CAR T Cell Migratory Behavior. In addition to static 3D stacks, TPLSM allows for real-time analysis of cellular migratory behavior within specified tumor regions in vivo. At early time points, intratumoral h19m28z CAR T cells migrated at a lower velocity compared with intratumoral mock CAR T cells (Fig. 4 *A*–*C* and Movie S3). However, starting 14 d after intracerebral injection, median velocity of intratumoral h19m28z CAR T cells increased over the following weeks (Fig. 4*C*). In the contralateral hemisphere (and hence, in absence of antigen), h19m28z and mock CAR T cells migrated at a similar velocity (Fig. 4*D*), indicating that CAR expression alone does not influence intracerebral migratory velocity. After tumor regression, h19m28z CAR T cells at the tumor injection site resumed migratory velocities similar to contralateral h19m28z CAR T cells, suggesting

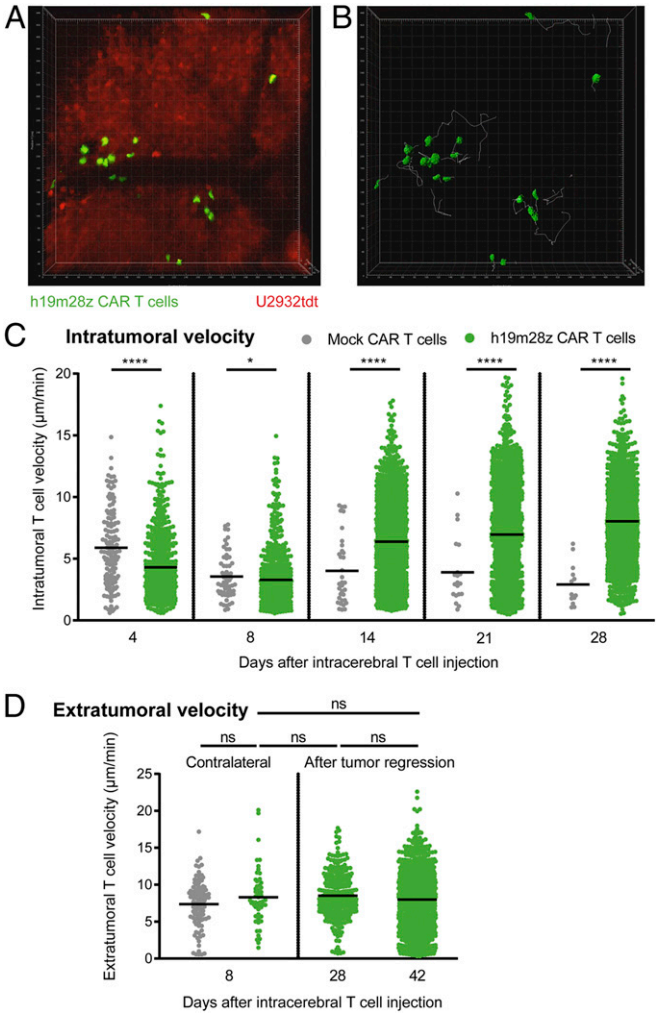

Fig. 4. Initially, intratumoral h19m28z CAR T cells migrate slower than mock CAR T cells in vivo, while extratumoral velocity shows no difference. (*A*) The 3D TPLSM stack of U2932tdt cells (red) and h19m28z CAR T cells (green) (Movie S3). Representative movie of 4 mice from 2 independent experiments. (*B*) The 3D reconstruction of CAR T cells (green) and their intratumoral migration tracks (white) during 30 min of a representative time-lapse TPLSM video 4 d after intracerebral CAR T cell injection. (*C*) Quantification of individual, intratumoral T cell velocities. Each point represents 1 CAR T cell track. Pooled results from time-lapse TPLSM videos of at least 30-min duration (recorded every 30 s) per time point. ROI of 450 × 450 × 66 μm starting at least 100 μm beneath the most superficial tumor compartment. Pooled data from 4 mice per group from 2 independent experiments. (*D*) Quantification of individual, extratumoral T cell velocities in the ROI contralateral (*Left*; $n = 4$ per group) or at tumor injection site after tumor regression (*Right*; $n = 2$ for h19m28z CAR T cell-treated mice). Results from 2 independent experiments. Data are shown as mean. Mann–Whitney *U* test. ns, not significant. $^*P < 0.05$; $^{****}P < 0.0001$.

that the initially lower velocity of intratumoral h19m28z CAR T cells is dependent on the presence of CD19 antigen. In h19m28z CAR T cell-treated mice, several intratumoral CAR T cell mitoses were visible (*SI Appendix*, Fig. S6 and Movie S4).

Effect of Intracerebral CAR T Cell Injection on Tumor Size. Starting 14 d after treatment, the visible 2-dimensional (2D) tumor area of mice treated with h19m28z CAR T was smaller compared with mock CAR T cell treatment (Fig. 5 *A* and *B*). h19m28z CAR T cell treatment led to complete tumor regression in 4 of 6 mice (66.7%), with only a small tumor (<1 mm^2) present in 1 mouse (16.7%). In only a single h19m28z CAR T cell-treated mouse (16.7%), a large (>1-mm^2) intracerebral tumor developed. However, in 4 of 5 (80%) animals receiving mock CAR T cells, we found large, intracerebral tumors (Fig. 5*A*).

CAR T Cell Function below Visualizable Depths. Repeated intravital TPLSM allowed reliable visualization of tumor tissue up to a depth of 400 μm. Nevertheless, the implantation of a chronic cranial window might induce an artificial tumor environment, potentially interfering with CAR T cell response. To validate our findings of successful tumor eradication, intratumoral T cell accumulation, and distribution, we repeated intracerebral CAR T cell injection in mice without a cranial window and performed ex vivo immunofluorescence microscopy 28 d after intracerebral T cell injection.

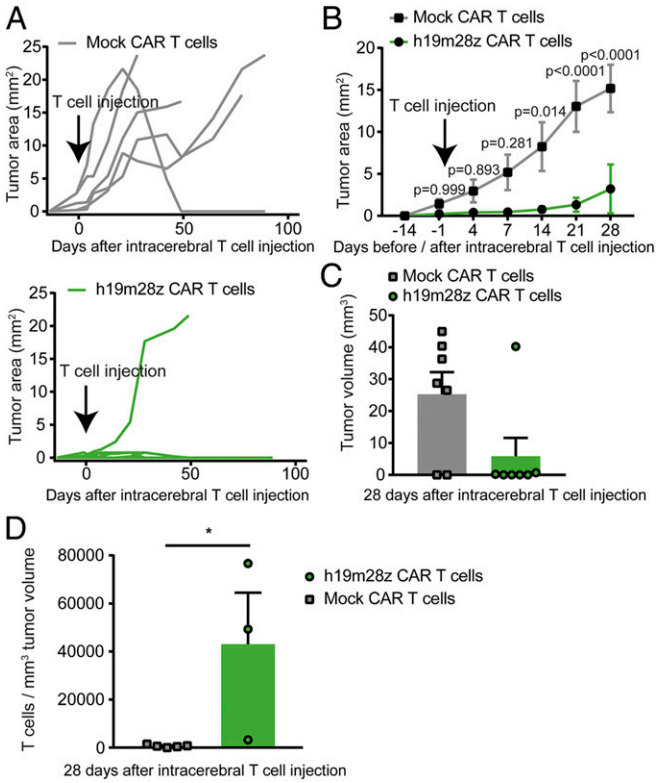

Fig. 5. Intracerebral injection of h19m28z CAR T cell treatment leads to reduced PCNSL growth, more tumor regressions, and a higher number of intratumoral CAR T cells compared with mock CAR T cell treatment. (*A* and *B*) Intracerebral, 2D tumor area assessed by in vivo microscopy after mock and h19m28z CAR T cell treatment. Individual (*A*) and pooled (*B*) tumor size. Results from 3 independent experiments. (*C*) Intracranial tumor volume measured via immunofluorescence 28 d after T cell injection in mock or h19m28z CAR T cell-treated mice without cranial window implantation (n = 7 per group from 2 independent experiments). (*D*) Intratumoral CAR T-cell number per 1 mm^3 tumor volume 28 d after intracerebral CAR T cell injection. (*A* and *B*) n = 5 and 6 mice for mock and h19m28z CAR T cell-treated mice, respectively. (*C* and *D*) n = 7 mice per group from 2 independent experiments. A 2-way ANOVA followed by Sidak's multiple comparisons test (*B*) or Mann–Whitney *U* test (*C* and *D*). Data are shown as mean ± SEM (*B*) or mean + SEM (*C* and *D*). *P < 0.05.

In mock CAR T cell-treated mice, a large tumor (>1 mm^3) developed in 5 of 7 mice (Fig. 5*C*); 2 of 7 mice showed no sign of intracranial tumor growth. As intracranial tumor growth could not be visually verified before random allocation to the treatment group, this could be either due to spontaneous intracranial tumor regression or due to unsuccessful tumor engraftment. In h19m28z CAR T cell-treated mice, only 1 of 7 mice developed a large intracranial tumor (>1 mm^3); 2 of 7 mice showed a small tumor (<1 mm^3) (Fig. 5*C*). These tumors were densely infiltrated with h19m28z CAR T cells (*SI Appendix*, Fig. S7), suggesting ongoing tumor regression; 4 of 7 mice showed no intracerebral tumor cells. In all mice with detectable tumor tissue (5 mock CAR T cell-treated mice, 3 h19m28z CAR T cell-treated mice), we compared intratumoral CAR T cell density. h19m28z CAR T cell-treated mice showed higher tumor infiltration than mock CAR T cell-treated mice, similar to the results obtained via TPLSM (Fig. 5*D*). h19m28z CAR T cells were not only visible at high numbers intratumorally but also, within the meninges, subependymally, and within the choroid plexus (*SI Appendix*, Fig. S7), whereas only low numbers of T cells were present in mock CAR T cell-treated mice (*SI Appendix*, Fig. S8).

To investigate the reasons for the enhanced infiltration capacity of h19m28z compared with mock CAR T cells, we utilized a platform for repetitive immunostaining of tissue sections via repetitive bleaching and antibody restaining (chip cytometry; Zellkraftwerk) (15). Based on this approach, of a set of various markers (Ly6G/C, CD11c, CD11b, CD4, CD8, CD27, CD3, CD44, Eomes, TCF1, KLRG1, CD103, CD49a, IRF4, CD69, and CD25), we identified 2 markers that yielded exciting results. Peri- and intratumoral mock CAR T cells remained almost universally positive for surface expression of CD27, while h19m28z CAR T cells virtually lacked CD27 expression (*SI Appendix*, Fig. S9). CD27 is a key differentiation marker in T cells, in which downregulation signifies differentiation of resting memory T cells into terminal effector T cells (16, 17). Furthermore, in mock CAR T cell-treated animals, numerous $CD11c^+$ cells can be found surrounding the intracerebral lymphoma, forming a highly interconnected mesh in close contact with remaining mock CAR T cells (*SI Appendix*, Fig. S10*A*). In h19m28z CAR T cell-treated animals, this phenomenon cannot be observed (*SI Appendix*, Fig. S10*B*).

Spatiotemporal Distribution of CAR T Cells during Tumor Regression. Four days after intracerebral injection, mock CAR T cells were detectable inside and around the cerebral tumor (Fig. 6*A*). After 14 d, intratumoral mock CAR T cells could still be seen. However, their intratumoral numbers diminished thereafter. In the example shown in Fig. 6*A*, tumor growth continued unimpeded during 4 wk, culminating in the development of a tumor with a greater than 3,000-μm diameter at day 28 extending into the contralateral brain hemisphere. In contrast, intracerebral h19m28z CAR T cell injection led to higher intra- and peritumoral CAR T cell numbers already at day 4 (Fig. 6*B*); 14 d after injection, intratumoral h19m28z CAR T cell number further increased. CAR T cell density peaked at day 21, while tumor size did not increase. In the example of Fig. 6*B*, PCNSL regressed at day 28, while h19m28z CAR T cells were still detectable numerously inside the tumor-free brain parenchyma for up to 159 d (Movies S5–S7).

Long-Term CAR T Cell Persistence. After tumor regression, intracranial h19m28z CAR T cells remained visible for up to 159 d after intracerebral injection without recurrence of tumor cells (Movies S5–S7). In 5 of 6 mice treated, intracranial h19m28z CAR T cells were detectable at the end of observation period (mean, 85 d; range, 35 to 159 d after CAR T cell injection), even

MEDICAL SCIENCES

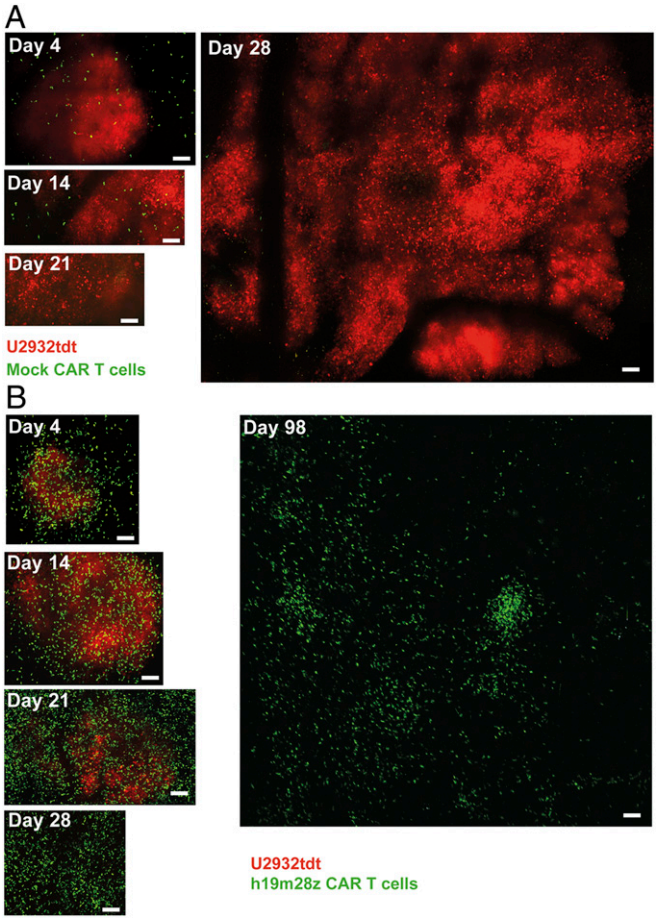

Fig. 6. Mock CAR T cells persist less than 3 wk intratumorally, and PCNSL grows unimpededly, while h19m28z CAR T cells eradicate intracerebral U2932tdt cells and persist intracerebrally for more than 14 wk after intracerebral injection. Representative, serial TPLSM images of intracerebral mock CAR T cells (*A*; green) or h19m28z CAR T cells (*B*; green) and U2932tdt cells (red). Mosaics of maximum intensity projections with dimensions of 450 × 450 × 400 μm per ROI (until day 28) or 2,387 × 2,387 × 280 μm (day 98) (Movie S5). $n = 4$ mice per group from 2 independent experiments. (Scale bars: 100 μm.)

if complete tumor regression occurred. In one animal, however, tumor regression occurred, and subsequently, neither h19m28z CAR T cells nor tumor cells were visible for 103 d. Additionally, in several h19m28z CAR T cell-treated mice, CAR T cells were detectable intravascularly in high numbers via epifluorescence microscopy (Movies S7 and S8). To validate this observation and to delineate the intravascular CAR T cell dynamics, we repeatedly performed blood analyses. Already 5 d after stereotactic, intracerebral injection, h19m28z CAR T cells were present in the blood circulation (Fig. 7*A*). At day 10, 5 of 7 mice showed intravascular h19m28z CAR T cells. In mock CAR T cell-treated mice, however, no intravascular T cells could be observed until day 25, indicating that h19m28z CAR T cells were able to intravasate faster compared with mock CAR T cells.

Furthermore, circulating CAR T cells were able to infiltrate lymph nodes 28 d after intracerebral injection. These CAR T cells were not only present in cervical, brain-draining lymph nodes but also, in inguinal, nondraining lymph nodes in high numbers, confirming that h19m28z CAR T cells successfully infiltrated secondary lymphoid organs via the bloodstream (Fig. 7 *B*–*D*). Mock CAR T cells were present at lower numbers in nondraining lymph nodes, suggesting a limited capability of these cells to enter lymph nodes via the bloodstream within 28 d.

Discussion

In this study, we developed a mouse model of PCNSL with intracerebral and periventricular tumor growth. Combining a chronic cranial window with repeated TPLSM, we were able to analyze PCNSL growth in unprecedented detail. Furthermore, we demonstrate that, after i.v. injection, CD19-specific CAR T cells infiltrate the tumor in low numbers, leading to tumor elimination in a fraction of mice. However, a single intracerebral injection of very low numbers of anti-CD19 CAR T cells led to a more rapid and sustained tumor infiltration and to successful elimination of large, established tumors in the majority of animals treated. Furthermore, we show the dynamics of intravasation and infiltration of CD19-specific CAR T cells into nondraining lymph nodes as well as their long-term intracerebral

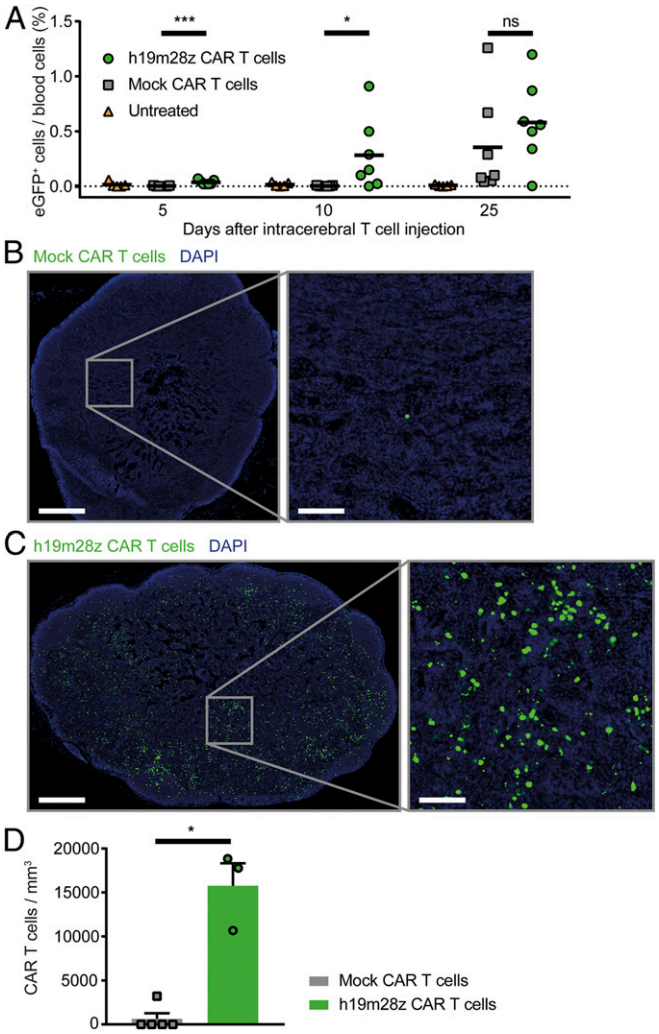

Fig. 7. After intracerebral injection, h19m28z CAR T cells intravasate earlier and infiltrate nondraining lymph nodes in higher numbers compared with mock CAR T cells. (*A*) Fraction of CAR T cells of all leukocytes in blood measured by FACS analysis (eGFP$^+$). Control (orange; $n = 5$), mock CAR T cells (gray; $n = 7$), and h19m28z CAR T cells (green; $n = 7$). Results from 2 independent experiments. (*B* and *C*) Representative immunofluorescence images of inguinal lymph nodes (mock [*B*] or h19m28z [*C*] CAR T cells [green] and 4′,6-diamidino-2-phenylindole (DAPI) [blue]). (*D*) Number of CAR T cells in inguinal lymph nodes of mice with intracerebral tumors present 28 d after T cell injection ($n = 5$ mock and 3 h19m38z CAR T cell-treated mice) (same animals as in Fig. 5*D*). Results from 2 independent experiments. Mann–Whitney *U* test. Data are shown as mean (*A*) and mean + SEM (*D*). ns, not significant. $^*P < 0.05$; $^{***}P < 0.001$.

and intravascular persistence for up to 159 d, which was associated with durable treatment response.

The most remarkable success of CAR T cells has been achieved in $CD19^+$ B cell malignancies. Many of these semiliquid hematological malignancies reside in the bone marrow, a niche easily accessible for intravascular T cells. In solid $CD19^+$ tumors, such as PCNSL, CAR T cells face 3 important, additional barriers: hindered migration toward the tumor, limited penetration into the tumor, and a highly immunosuppressive tumor microenvironment (9, 18), none of which have been visualized in vivo at single-cell resolution before. Additionally, CAR T cell trials have lacked the possibility to repeatedly assess the detailed cellular dynamics at the exact same tumor site. These limitations have been overcome in our mouse model using a chronic cranial window.

Most preclinical studies of CAR T cells have used human CAR T cells. However, several human cytokines lack activity on murine receptors (such as human IFN-γ, human GM-cerebrospinal fluid (CSF), or human IL-3 on murine receptors) and vice versa (such as murine IL-6 on human receptors) (19–21). Thus, thorough analysis of many cellular aspects of CAR T cells is precluded in models using human CAR T cells. To address these concerns, we used a CAR with a murine scFv combined with murine costimulatory molecules in syngeneic T cells, enhancing the comparability with the clinical situation of autologous CAR T cells.

Current clinical trials use both intracranial and i.v. application of CAR T cells to treat brain tumors, as the optimal route of delivery remains unclear. In several preclinical tumor models (including brain tumors), regional injection has led to earlier CAR T cell activation, higher efficacy, and longer persistence compared with i.v. injection (22–24). However, intracerebral injection in patients with symptomatic brain tumors carries an elevated procedural risk compared with i.v. application. Furthermore, a case report has recently been published of a patient suffering from systemic DLBCL with a secondary, intracerebral lymphoma manifestation, which completely regressed after i.v. anti-CD19 CAR T cell injection, suggesting a potentially favorable effect of i.v. CAR T cell delivery in CNS lymphoma (8). In our model of PCNSL, however, i.v. application of 3.5×10^5 CAR T cells resulted in a lower rate of PCNSL regression compared with intracerebral injection. Intracerebral injection of as few as 2×10^4 h19m28z CAR T cells led to complete eradication of large, established tumors and to long-term survival. Preclinical studies using i.v.-injected CAR T cells to treat cancer used highly varying doses of CAR T cells (1×10^5 to 30×10^6 human T cells) (19, 25, 26). However, doses used for regional applications (e.g., intrapleural injections) proved to be efficacious at doses as low as 3×10^4 injected CAR T cells, vastly outperforming i.v.-injected CAR T cells (22). These findings corroborate the high efficacy of intracerebrally injected CAR T cells seen in our experiments.

Our model allowed us to dissect the spatiotemporal pattern of CAR T cell accumulation. After i.v. application, a delayed and comparatively poor infiltration of 19m28z and mock CAR T cells in PCNSL can be seen, starting 14 d after injection. Intracerebral injection, however, led to earlier and more sustained peritumoral accumulation of h19m28z and mock CAR T cells starting already 4 d after injection. Furthermore, we found a striking difference in infiltration patterns. Mock CAR T cells primarily accumulated at the tumor borders and in the subarachnoid space, where T cell immune surveillance is physiologically located (27), whereas h19m28z CAR T cells were found to significantly outnumber mock CAR T cells and were shown to infiltrate deeper tumor regions. Reasons for the earlier, more sustained, and more abundant presence of intratumoral h19m28z CAR T cells remain speculative and probably rely on several different mechanisms. These likely include enhanced intratumoral proliferation and survival of intracranial-injected h19m28z CAR T cells due to early antigen contact and resulting CAR signaling, which affects CAR T cell differentiation, proliferation, and survival. In line with this, we found that tumor-associated h19m28z CAR T cells were mainly CD27-negative terminal effector T cells; mock CAR T cells, however, retained CD27 positivity. Furthermore, the composition of the tumor stroma may affect the tumor infiltration of (CAR) T cells. In mice treated with mock CAR T cells, $CD11c^+$ myeloid cells formed a dense rim around the tumor. In close association, we found $CD3^+$ T cells. In mice treated with h19m28z, however, we rarely found $CD11c^+$ cells at the tumor borders (*SI Appendix*, Fig. S10). It has been reported that $CD11c^+$ myeloid cells engage T cells in long-lasting, unproductive interactions, serving as a functional barrier to an effective T cell response (28–31). However, further experiments are needed to confirm the potential role of these preliminary observations.

In addition to analysis of CAR T cell infiltration, our model allowed for dynamic dissection of intratumoral and intracerebral CAR T cell velocities. During the first 8 d, low intratumoral velocities and a higher number of stationary h19m28z CAR T cells were observed. Over time, however, CAR T cell velocity increased. T cell velocities are linked to effector functions, and reduced velocities are seen when T cells form an immunological synapse (IS) with tumor cells to release perforin and granzymes at the contact site (32). At an early phase of tumor rejection, TCR-mediated antitumor cytotoxicity is associated with reduced T cell velocity (4 ± 2 μm/min) due to long-lasting contacts with tumor cells (11, 12, 33). Similar to our observation, at late stages of tumor rejection, intratumoral T cells expressing tumor-specific TCRs resume higher velocities (8 ± 3 μm/min) (11). Continuous tumor cell killing may explain this increase in velocity over time. As the density of viable tumor cells decreases, fewer ISs are being formed, thus potentially increasing average velocity of intratumoral CAR T cells.

CAR T cells have been shown to sequentially contact and kill several tumor cells, with faster formation of an IS and more rapid detachment of tumor cells compared with TCR-mediated cytotoxicity (34, 35). Therefore, while exerting cytotoxic function, CAR T cell velocity may exhibit higher intratumoral velocities. However, the velocities observed in our model were similar to those of T cells expressing tumor-specific TCRs seen in peripheral tumors (11), although comparability across different studies, in different tumors, and in different target organs remains limited. In general, CAR T cell velocity is possibly influenced by a multitude of factors, including tumor antigen expression, CAR expression, scFv affinity, costimulatory signaling, and T cell phenotype as well as tumor-derived immunosuppressive factors.

Furthermore, our results show that, after intratumoral accumulation, h19m28z CAR T cells are able to enter the bloodstream and infiltrate nondraining lymph nodes. It remains to be seen if lymph node infiltration is a prerequisite for successful tumor eradication or a mere consequence of blood infiltration, especially after the importance of lymphatics and brain-draining cervical lymph nodes in the immune surveillance of the brain has been shown (36, 37).

Our study has some limitations. With the use of $Foxn1^{nu/nu}$ mice, we chose an animal model devoid of functional T cells. However, in contrast to widely used NOD scid gamma mice, these mice retain full macrophage, B cell, and NK cell function (38). The absence of functional T cells successfully enabled us to study U2932 cell xenografts, a $CD19^+$ human DLBCL cell line. Furthermore, the lack of endogenous T cells in this mouse model facilitates the successful engraftment of syngeneic CAR T cells, obviating the need for lymphodepletion regimens, such as total body irradiation or cyclophosphamide (39–42). Both of these lymphodepletion strategies could significantly impair the growth of PCNSL, which is known for its high radio- and chemosensitivity. However, as $Foxn1^{nu/nu}$ mice are devoid of functional T cells, the efficacy of CAR T cells might be overestimated, as endogenous regulatory T cells could limit the efficacy of CAR T cells (42, 43). Another potential limitation of this

mouse model is the possible contribution of xenoimmunity to the potent antitumor efficacy of CAR T cells in our model. As Foxn1$^{nu/nu}$ mice retain fully functional NK cells, an additive contribution of NK cells to successful tumor eradication during h19m28z CAR T cell therapy cannot be excluded.

Furthermore, injection of syngeneic, functional T cells into these mice could abrogate the immune deficit, thereby possibly contributing to the antitumor efficacy via the graft-vs.-lymphoma effect. Although we have not seen relevant antitumor cytotoxicity of mock CAR T cells in vitro, we compared h19m28z CAR T cells with mock CAR T cells to control for graft-vs.-tumor effects in vivo. Indeed, in one of our mice, we saw complete regression of an established PCNSL in the mock CAR T cell-treated group, suggesting that T cell reestablishment in mice retaining functional NK cells can be enough for PCNSL xenograft rejection in rare cases.

In addition, preparation of a chronic cranial window represents an invasive surgical procedure and may lead to mechanical damage of the arachnoid mater. Furthermore, it might cause sterile injury responses with microglial activation and astrogliosis, potentially impacting both CAR T cell response and their intracranial localization. Although these inflammatory reactions have been reported to be transient in nature (44, 45), we cannot formally exclude the possibility that some inflammatory responses extend beyond day 14. Therefore, we cannot rule out that meningeal and/or parenchymal inflammation might affect both CAR T cell positioning to the most superficial aspects of the brain and their migration toward the tumor. However, these sterile injury responses are present in both groups injected with either mock CAR or h19m28z CAR T cells, indicating that this inflammatory response alone is unlikely sufficient to induce T cell infiltration into the tumor in high numbers.

One potential limitation of i.v. delivery of CAR T cells in our mouse model is its reduced translatability to the clinical setting of PCNSL: in humans, i.v.-delivered anti-CD19 CAR T cells receive early activation through contact with intravascular CD19$^+$ B cells, dramatically shortening time to antigen exposure and subsequent CAR T cell activation and proliferation. As the murine, anti-human CD19 CAR T cells used in our experiment do not cross-react to murine CD19$^+$ B cells, duration to antigen exposure is increased compared with the clinical setting, leading to potential underestimation of i.v. treatment efficacy in our model.

Recently, a single case of a patient with recurrent IL13Rα2-positive multifocal glioblastoma has been reported, in which tumor resection was followed by repeated intracavitary and intraventricular injections of IL13Rα2-specific CAR T cells (46). This led to complete remission of all lesions, including the intraspinal metastases. Although in this patient, glioblastoma eventually recurred (with lower IL13Rα2-expression), these results illustrate the feasibility and the potential success of intracranial CAR T cell injections even in patients suffering from widespread, multifocal, high-grade brain cancer. Consequentially, several clinical trials for brain tumors, such as glioblastoma (e.g., NCT02442297, NCT03283631), evaluate intracranial (intratumoral, intracavitary, or intraventricular) injections to overcome trafficking through the blood–brain and blood–CSF barriers. Additionally, regional delivery allows for injection of lower CAR T cell numbers compared with i.v. injection, possibly reducing the risk of side effects.

Moreover, our results demonstrate that, even after local parenchymal injection, CAR T cells are able to infiltrate into the contralateral, "healthy" brain hemisphere. Therefore, as PCNSL usually presents as a whole-brain disease with widespread individual tumor cells, regional CAR T cell injection enables trafficking of these cells even toward asymptomatic, smaller intracranial tumor sites behind potentially intact blood–brain barriers.

Since most PCNSLs are routinely diagnosed via stereotactic biopsy, stereotactic injection should be similarly feasible. Furthermore, as 95% of PCNSL have direct contact to the subarachnoid space and hence, the cerebrospinal fluid (47), intraventricular injection via Ommaya reservoirs could offer a safe alternative for repeated CAR T cell injections.

Taken together, our results demonstrate the efficacy of intracranially injected CD19-specific CAR T cells even in large, established PCNSL. Based on these results and on the encouraging results of other groups, clinical trials in patients with refractory CD19$^+$ PCNSL are highly warranted.

Materials and Methods

Cell Lines. U2932, a human DLBCL cell line, was provided by Martin Dreyling, Ludwig Maximilians University, Munich, Germany. Cell line authentication was performed using short tandem repeat profiling at German Collection of Microorganisms and Cell Cultures (Deutsche Sammlung von Mikroorganismen und Zellkulturen), Germany. U2932 cells were cultured in Iscove's Modified Dulbecco's medium supplemented with 20% human plasma, 0.4% heparin, and 0.1% beta-mercaptoethanol or RPMI 1640 supplemented with 10% fetal bovine serum. All cells were regularly tested for mycoplasma infection using the PCR *Mycoplasma* Test Kit (PanReac AppliChem GmbH). To keep genetic drift to a minimum, cells were maintained in culture for a maximum duration of 2 to 3 mo after thawing.

TdTomato Vector. A PCR product containing the coding sequence of tdTomato (vector ptdTomato; catalog no. 632531; TaKaRa Clontech) was cloned into the lentiviral expression vector pLVX-IRES-neoR (Lenti X Bicistronic Expression System; catalog no. 632181; TaKaRa Clontech). The resulting construct pLVX-tdTomato-IRES-Neo was verified by restriction enzyme digest and Sanger sequencing.

Electroporation. To stably transfect U2932 cells, the pLVX-tdTomato-IRES-Neo vector was electroporated using the Gene Pulser Xcell system (Bio-Rad Laboratories). Immediately after electroporation, cells were resuspended in prewarmed (37 °C), CO_2-equilibrated medium; 24 h after electroporation, selection medium containing 800 μg/mL G418 was added.

Fluorescence-Activated Cell Sorting (FACS) and Cell Sorting. Flow cytometry and cell sorting were performed on a MoFlo Astrios Cell Sorter (Beckman Coulter). Briefly, lymphoma cells were measured for tdTomato expression by flow cytometry; 1 to 5% of the cells with the highest level of tdTomato expression were repeatedly FACS sorted until tdTomato expression was high enough for TPLSM. Cells with sufficient levels of tdTomato expression were frozen in culture medium with 10% (vol/vol) dimethyl sulfoxide and kept at −80 °C until use. Flow cytometry for blood analysis was performed on a CyAn XDP (Beckmann Coulter) or a FACSAria (BD Biosciences).

Retroviral CAR Vectors. The second generation murine m1928z CAR vector was modified to contain a murine anti-human CD19 scFv (derived from clone FMC63 [48]) and fused via a CD8-derived extracellular and transmembrane domain to the intracellular CD28 costimulatory domain and the CD3ζ signaling domain into the retroviral pMP71 vector (provided by Wolfgang Uckert, Max Delbrück Center, Berlin, Germany). For selection (cell sorting), this gene construct is connected via a P2A linker to a truncated, functionally inert version of the epidermal growth factor receptor (EGFRt; provided by Stanley Riddell, Fred Hutchinson Cancer Research Center, Seattle, WA), resulting in the h19m28z vector. For mock CAR T cells, the scFv domain has been removed from the m1928z construct before cloning. eGFP was cloned into both pMP71 retroviral vectors (49).

T Cell Isolation and Transduction. Primary NMRI Foxn1$^{nu/+}$ T cells were isolated and transduced as described (50). Briefly, splenocytes were isolated from spleens of heterozygous NMRI Foxn1$^{nu/+}$ mice; cultured in RPMI 1640 containing 10% fetal calf serum (FCS), 0.025% L-glutamine, 0.1% Hepes, 0.001% gentamicin, and 0.002% streptomycin supplemented with 25 U/mL IL-2; and stimulated overnight with anti-mouse CD3 antibodies (1:1,000, clone 145–2C11; BD Pharmingen) and anti-mouse CD28 antibodies (1:5,000, clone 37.51; BD Pharmingen). After retroviral transduction and expansion, transduced T cells were sorted using a MoFloII Cell Sorter (Beckman Coulter) or FACSAria (BD Biosciences) on double positivity (eGFP and EGFRt positivity) by addition of a reversible anti-EGFRt FAB-Streptamer and Strep-Tactin APC (IBA) after excluding CD19$^+$ B cells (aCD19mAB, clone 1D3, PECF594; BD Pharmingen) and dead cells (propidium iodide; Invitrogen). Anti-EGFRt FAB-Streptamer has been removed by addition of 2 mM D-Biotin (IBA).

xCELLigence Cytotoxicity Assay (ACEA). Blanks of specific 96-well E-Plates (ACEA; Biosciences, Inc.) with DMEM containing 10% FCS, 0.025% L-glutamine, and 0.002% streptomycin were measured by the xCELLigence real-time cell analysis instrument (ACEA, Biosciences, Inc.); 2×10^4 HEK293-CD19$^+$ target cells were seeded into a 96-well E-Plate and cultured for 24 h. Transduced and purified h19m28z CAR/eGFP$^+$ or mock CAR/eGFP$^+$ T cells were added to the target cells in effector to target ratios of 10:1, 5:1, and 2.5:1. Plates were incubated for 3 d while measuring impedance to monitor real-time killing capacity. Specific lysis was calculated as follows:

$$\textit{Percentage of cytolysis} = ((\textit{Cell Index}_{\textit{no effector}} - \textit{Cell Index}_{\textit{effector}}) / \textit{Cell Index}_{\textit{no effector}}) \times 100.$$

Study Design. All treatments were randomly allocated, and all experiments and quantifications were conducted by an investigator blinded to treatment allocation.

Mice. We used homozygous male NMRI Foxn1$^{nu/nu}$ mice (Charles River Laboratories) at the age of 8 to 14 wk for tumor implantation experiments. Heterozygous male NMRI Foxn1$^{nu/+}$ mice were used for T cell isolation. All animal research was conducted in accordance with the animal welfare act and the Bavarian state regulations for animal experimentation. Protocols were approved by the state authorities (Regierung von Oberbayern, Germany).

Surgical Procedures and Perioperative Care. Microsurgical implantation of a chronic cranial window and stereotactic tumor cell injection were performed as previously described (51, 52). Briefly, a circular part of the cranium (diameter of 5.5 mm) was removed using a sterile carbon steel microdrill. To achieve optimal contrast and resolution during serial imaging, the dura mater was removed to avoid dural fibrosis. The dura mater was separated from the leptomeninges using 2 thin forceps and removed (except in the region demarcating the sagittal sinus). A sterile round cover glass and a custom-made ring (polyether ether ketone [PEEK]) were firmly attached to the cranial bone using acrylic dental glue (Cyano veneer); 2.5×10^5 U2932tdt cells were resuspended in 1 to 2 μL Dulbecco's phosphate-buffered saline (DPBS) and stereotactically injected at predefined stereotactic coordinates (1 mm lateral and 2 mm posterior to the bregma at an intraparenchymal depth of 1.5 mm) either after careful removal of the cranial window (in vivo analysis) or through a borehole (immunofluorescent analysis). Before CAR T cell injection, mice were randomized to treatment groups 14 d after tumor implantation. For i.v. injection, 3.5×10^5 h19m28z or mock CAR T cells were concentrated in 100 to 200 μL DPBS and injected into the tail vein. For intracerebral injections, 5×10^4 h19m28z mock CAR T cells were concentrated in 0.5 to 1.2 μL DPBS and stereotactically injected 1 mm posterior to the tumor injection point at an intraparenchymal depth of 1.5 mm. In mice without a cranial window, tumor presence could not be confirmed before CAR T cell injection. In these mice, a lower number of cells (2×10^4 h19m28z or mock CAR T cells) was stereotactically injected 1 mm posterior to the tumor injection point at an intraparenchymal depth of 1.5 mm. To analyze intravascular CAR T cell numbers, blood sampling of the facial vein was performed at days 5, 10, and 25 after intracerebral T cell injection of 2×10^4 CAR T cells. The facial vein was punctured using a small lancet, and blood drops were collected in ethylenediaminetetraacetic acid-coated capillary tubes.

Two-Photon Laser Scanning Microscopy. For TPLSM, a Multiphoton TrimScope I system (LaVision BioTec) connected to an upright Olympus microscope equipped with a MaiTai Laser (690 to 1,040 nm; Spectra Physics) and a 20× water immersion objective (numerical aperture [NA] 0.95; Olympus XLUMPlanFl) or a 4× objective (NA 0.28; Olympus XLFluor 4×/340) was used. During microscopy, mice were anesthetized using isoflurane in oxygen at a concentration of 1.0 to 2.0% adjusted according to breathing rate. During imaging, the PEEK ring was tightly secured into a custom-built fixation device. For visualization of cerebral vessels, 0.1 mL fluorescein isothiocyanate (FITC)-dextran (2 MDa molecular mass) was injected i.v. at a concentration of 10 mg/mL.

Image Analysis. For image analysis, ImageJ/Fiji and Imaris (Bitplane AG) were used. To calculate tumor size using intravital microscopy, the 2D tumor area was calculated based on the diameters (anterior–posterior and left–right) during epifluorescence microscopy according to the following formula:

$$\text{area} = \pi \times \text{length}/2 \times \text{width}/2.$$

If more than 1 tumor was visible, individual tumor areas were added.

Immunofluorescence Analyses. A complete list of antibodies used is in *SI Appendix*. After staining of 15-μm cryosections spaced 495 μm apart, immunofluorescent pictures were taken on a BX60 upright microscope (Olympus). Tumor areas were manually delineated using Axiovision software (Carl Zeiss Microscopy). If multiple tumors were present on one slice, individual tumor areas were added. Total tumor area per slice was multiplied with a thickness of 495 μm. Addition of all values yielded total tumor volume. To determine intratumoral CAR T cell density, mosaics of these cryosections were taken on a Zeiss AxioImager.M2 upright microscope (Carl Zeiss Microscopy). Intratumoral CAR T cells were counted and divided by the total volume of tumor in this cryosection (2D tumor area multiplied by 0.015). To determine CAR T cell density in lymph nodes, 15-μm cryosections of inguinal lymph nodes of mice with intracerebral tumor present were created. After creating mosaics, 3 regions measuring 500 × 500 μm were randomly allocated, and CAR T cell density was measured using Axiovision software.

Chip Cytometry. Chip cytometry was performed as described before (15) on the ZellScanner ONE system (Zellkraftwerk GmbH) consisting of a modified Zeiss Axio Observer inverted microscope using HBO illumination and a Plan-Neofluar 20×/0.5 objective (Carl Zeiss Microscopy). Briefly, 15-μm cryosections were mounted on ZellSafe tissue chips and washed with degassed PBS to remove embedding medium. Tissue sections were stained with monoclonal antibodies (*SI Appendix*) at the indicated concentrations in degassed PBS. After washing, fluorescence images of each position were acquired followed by automated bleaching through extended excitation. This process was repeated for each set of biomarkers. Resulting images were corrected for background fluorescence (acquired before staining).

Statistical Analyses. Data are expressed as mean, mean + SEM, or mean ± SEM as indicated. Statistical analysis was performed using GraphPad Prism v7.02. For comparison of 2 groups, the Mann–Whitney *U* test was used; for repeated measures, a 2-way ANOVA was used followed by Sidak's multiple comparisons test as indicated. A level of $P < 0.05$ was considered significant: $^*P < 0.05$, $^{**}P < 0.01$, $^{***}P < 0.001$, and $^{****}P < 0.0001$.

Data Availability. All additional data (materials, associated protocols) will be made available to readers upon request.

ACKNOWLEDGMENTS. We thank S. Massberg for helpful discussions and the SFB 914 (Project Z01/Steffen Massberg [S.M.]; Hellen Ishikawa-Ankerhold [H.I-A.]) for providing the infrastructure for animal experiments and TPLSM. We also thank the Flow Cytometry Unit of Technical University Munich for support during cell sorting. M.M. received funding from Friedrich-Baur-Foundation Grant 61/17 and European Federation of Neurological Societies Scientific Fellowship 2014. For this project, L.v.B. received funding from Else Kröner Fresenius Foundation Grant 2014_A265, the Bavarian Foundation for Gender Equality, and Foundation for Research and Teaching Grant 863.

1. M. S. Shiels *et al*., Trends in primary central nervous system lymphoma incidence and survival in the U.S. *Br. J. Haematol.* **174**, 417–424 (2016).
2. G. Fossard *et al*., Utility of post-therapy brain surveillance imaging in the detection of primary central nervous system lymphoma relapse. *Eur. J. Cancer* **72**, 12–19 (2017).
3. R. Ben Abdelwahed Bagga *et al*., Mouse models of primary central nervous system lymphomas: Tools for basing funding and therapeutic strategies. *J. Neurooncol.* **121**, 9–18 (2015).
4. A. D. Fesnak, C. H. June, B. L. Levine, Engineered T cells: The promise and challenges of cancer immunotherapy. *Nat. Rev. Cancer* **16**, 566–581 (2016).
5. D. L. Porter *et al*., Chimeric antigen receptor T cells persist and induce sustained remissions in relapsed refractory chronic lymphocytic leukemia. *Sci. Transl. Med.* **7**, 303ra139 (2015).
6. J. N. Kochenderfer *et al*., Chemotherapy-refractory diffuse large B-cell lymphoma and indolent B-cell malignancies can be effectively treated with autologous T cells expressing an anti-CD19 chimeric antigen receptor. *J. Clin. Oncol.* **33**, 540–549 (2015).
7. I. Cordone *et al*., Brain stereotactic biopsy flow cytometry for central nervous system lymphoma characterization: Advantages and pitfalls. *J. Exp. Clin. Cancer Res.* **35**, 128 (2016).
8. J. S. Abramson *et al*., Anti-CD19 CAR T cells in CNS diffuse large-B-cell lymphoma. *N. Engl. J. Med.* **377**, 783–784 (2017).
9. C. S. M. Yong *et al*., CAR T-cell therapy of solid tumors. *Immunol. Cell Biol.* **95**, 356–363 (2017).
10. C. Schläger *et al*., Effector T-cell trafficking between the leptomeninges and the cerebrospinal fluid. *Nature* **530**, 349–353 (2016).

11. A. Boissonnas, L. Fetler, I. S. Zeelenberg, S. Hugues, S. Amigorena, In vivo imaging of cytotoxic T cell infiltration and elimination of a solid tumor. *J. Exp. Med.* **204**, 345–356 (2007).
12. B. Breart, F. Lemaître, S. Celli, P. Bousso, Two-photon imaging of intratumoral CD8+ T cell cytotoxic activity during adoptive T cell therapy in mice. *J. Clin. Invest.* **118**, 1390–1397 (2008).
13. J. Deguine, B. Breart, F. Lemaître, J. P. Di Santo, P. Bousso, Intravital imaging reveals distinct dynamics for natural killer and CD8(+) T cells during tumor regression. *Immunity* **33**, 632–644 (2010).
14. M. Cazaux *et al*., Single-cell imaging of CAR T cell activity in vivo reveals extensive functional and anatomical heterogeneity. *J. Exp. Med.* **216**, 1038–1049 (2019).
15. L. M. Roesner *et al*., α-NAC-Specific autoreactive CD8+ T cells in atopic dermatitis are of an effector memory type and secrete IL-4 and IFN-γ. *J. Immunol.* **196**, 3245–3252 (2016).
16. T. H. Watts, TNF/TNFR family members in costimulation of T cell responses. *Annu. Rev. Immunol.* **23**, 23–68 (2005).
17. D. Hamann *et al*., Evidence that human CD8+CD45RA+CD27- cells are induced by antigen and evolve through extensive rounds of division. *Int. Immunol.* **11**, 1027–1033 (1999).
18. K. Newick, S. O'Brien, E. Moon, S. M. Albelda, CAR T cell therapy for solid tumors. *Annu. Rev. Med.* **68**, 139–152 (2017).
19. T. Giavridis *et al*., CAR T cell-induced cytokine release syndrome is mediated by macrophages and abated by IL-1 blockade. *Nat. Med.* **24**, 731–738 (2018).
20. A. Raziuddin *et al*., Receptors for human alpha and beta interferon but not for gamma interferon are specified by human chromosome 21. *Proc. Natl. Acad. Sci. U.S.A.* **81**, 5504–5508 (1984).
21. M. G. Manz, Human-hemato-lymphoid-system mice: Opportunities and challenges. *Immunity* **26**, 537–541 (2007).
22. P. S. Adusumilli *et al*., Regional delivery of mesothelin-targeted CAR T cell therapy generates potent and long-lasting CD4-dependent tumor immunity. *Sci. Transl. Med.* **6**, 261ra151 (2014).
23. S. J. Priceman *et al*., Regional delivery of chimeric antigen receptor-engineered T cells effectively targets HER2^{+} breast cancer metastasis to the brain. *Clin. Cancer Res.* **24**, 95–105 (2018).
24. A. Nellan *et al*., Durable regression of Medulloblastoma after regional and intravenous delivery of anti-HER2 chimeric antigen receptor T cells. *J. Immunother. Cancer* **6**, 30 (2018).
25. Z. Zhao *et al*., Structural design of engineered costimulation determines tumor rejection kinetics and persistence of CAR T cells. *Cancer Cell* **28**, 415–428 (2015).
26. Y. Kagoya *et al*., A novel chimeric antigen receptor containing a JAK-STAT signaling domain mediates superior antitumor effects. *Nat. Med.* **24**, 352–359 (2018).
27. S. S. Ousman, P. Kubes, Immune surveillance in the central nervous system. *Nat. Neurosci.* **15**, 1096–1101 (2012).
28. J. J. Engelhardt *et al*., Marginating dendritic cells of the tumor microenvironment cross-present tumor antigens and stably engage tumor-specific T cells. *Cancer Cell* **21**, 402–417 (2012).
29. A. Boissonnas *et al*., CD8+ tumor-infiltrating T cells are trapped in the tumor-dendritic cell network. *Neoplasia* **15**, 85–94 (2013).
30. E. Peranzoni *et al*., Macrophages impede CD8 T cells from reaching tumor cells and limit the efficacy of anti-PD-1 treatment. *Proc. Natl. Acad. Sci. U.S.A.* **115**, E4041–E4050 (2018).
31. D. G. DeNardo, B. Ruffell, Macrophages as regulators of tumour immunity and immunotherapy. *Nat. Rev. Immunol.* **19**, 369–382 (2019).
32. L. Martínez-Lostao, A. Anel, J. Pardo, How do cytotoxic lymphocytes kill cancer cells? *Clin. Cancer Res.* **21**, 5047–5056 (2015).
33. P. Mrass *et al*., Random migration precedes stable target cell interactions of tumor-infiltrating T cells. *J. Exp. Med.* **203**, 2749–2761 (2006).
34. A. J. Davenport *et al*., CAR-T cells inflict sequential killing of multiple tumor target cells. *Cancer Immunol. Res.* **3**, 483–494 (2015).
35. A. J. Davenport *et al*., Chimeric antigen receptor T cells form nonclassical and potent immune synapses driving rapid cytotoxicity. *Proc. Natl. Acad. Sci. U.S.A.* **115**, E2068–E2076 (2018).
36. A. Aspelund *et al*., A dural lymphatic vascular system that drains brain interstitial fluid and macromolecules. *J. Exp. Med.* **212**, 991–999 (2015).
37. A. Louveau *et al*., Structural and functional features of central nervous system lymphatic vessels. *Nature* **523**, 337–341 (2015).
38. S. Goyama, M. Wunderlich, J. C. Mulloy, Xenograft models for normal and malignant stem cells. *Blood* **125**, 2630–2640 (2015).
39. J. H. Sampson *et al*., EGFRvIII mCAR-modified T-cell therapy cures mice with established intracerebral glioma and generates host immunity against tumor-antigen loss. *Clin. Cancer Res.* **20**, 972–984 (2014).
40. G. Kueberuwa, M. Kalaitsidou, E. Cheadle, R. E. Hawkins, D. E. Gilham, CD19 CAR T cells expressing IL-12 eradicate lymphoma in fully lymphoreplete mice through induction of host immunity. *Mol. Ther. Oncolytics* **8**, 41–51 (2017).
41. L. Gattinoni *et al*., Removal of homeostatic cytokine sinks by lymphodepletion enhances the efficacy of adoptively transferred tumor-specific CD8+ T cells. *J. Exp. Med.* **202**, 907–912 (2005).
42. J. C. Lee *et al*., In vivo inhibition of human CD19-targeted effector T cells by natural T regulatory cells in a xenotransplant murine model of B cell malignancy. *Cancer Res.* **71**, 2871–2881 (2011).
43. C. M. Suryadevara *et al*., Preventing lck activation in CAR T cells confers Treg resistance but requires 4-1BB signaling for them to persist and treat solid tumors in nonlymphodepleted hosts. *Clin. Cancer Res.* **25**, 358–368 (2019).
44. A. Holtmaat *et al*., Long-term, high-resolution imaging in the mouse neocortex through a chronic cranial window. *Nat. Protoc.* **4**, 1128–1144 (2009).
45. G. J. Goldey *et al*., Removable cranial windows for long-term imaging in awake mice. *Nat. Protoc.* **9**, 2515–2538 (2014).
46. C. E. Brown *et al*., Regression of glioblastoma after chimeric antigen receptor T-cell therapy. *N. Engl. J. Med.* **375**, 2561–2569 (2016).
47. W. Küker *et al*., Primary central nervous system lymphomas (PCNSL): MRI features at presentation in 100 patients. *J. Neurooncol.* **72**, 169–177 (2005).
48. I. C. Nicholson *et al*., Construction and characterisation of a functional CD19 specific single chain Fv fragment for immunotherapy of B lineage leukaemia and lymphoma. *Mol. Immunol.* **34**, 1157–1165 (1997).
49. B. Engels *et al*., Retroviral vectors for high-level transgene expression in T lymphocytes. *Hum. Gene Ther.* **14**, 1155–1168 (2003).
50. P. J. Paszkiewicz *et al*., Targeted antibody-mediated depletion of murine CD19 CAR T cells permanently reverses B cell aplasia. *J. Clin. Invest.* **126**, 4262–4272 (2016).
51. L. von Baumgarten *et al*., Bevacizumab has differential and dose-dependent effects on glioma blood vessels and tumor cells. *Clin. Cancer Res.* **17**, 6192–6205 (2011).
52. Y. Kienast *et al*., Real-time imaging reveals the single steps of brain metastasis formation. *Nat. Med.* **16**, 116–122 (2010).
53. R. Bakker, P. Tiesinga, R. Kötter, The scalable brain atlas: Instant web-based access to public brain atlases and related content. *Neuroinformatics* **13**, 353–366 (2015).
54. P. Majka, E. Kublik, G. Furga, D. K. Wojcik, Common atlas format and 3D brain atlas reconstructor: infrastructure for constructing 3D brain atlases. Neuroinformatics 10(2):181–197 (2012).
55. G. A. Johnson *et al*., Waxholm space: an image-based reference for coordinating mouse brain research. Neuroimage 53(2):365–372 (2010).